Chinese Chemical Letters 31 (2020) 2177–2188

Contents lists available at ScienceDirect

Chinese Chemical Letters

journal homepage: www.elsevier.com/locate/cclet

Review

Research progress on transition metal oxide based electrode materials for asymmetric hybrid capacitors

Meizhen Dai, Depeng Zhao, Xiang Wu*

School of Materials Science and Engineering, Shenyang University of Technology, Shenyang 110870, China

ARTICLE INFO

Article history:
Received 3 January 2020
Received in revised form 8 February 2020
Accepted 12 February 2020
Available online 13 February 2020

Keywords:
Supercapacitors
Transition metal oxide
Electrochemical performance
Energy density
Power density
Storage mechanism

ABSTRACT

In the past few years, the increasing energy consumption of traditional fossil fuels has posed a huge threat to human health. It is very imperious to develop the sustainable and renewable energy storage and conversion devices with low cost and environment friendly features. Hybrid supercapacitors are emerging as one of the promising energy devices with high power density, fast charge-discharge process and excellent cycle stability. However, morphology and structure of the electrode materials exert serious effect on their electrochemical performances. In this review, we summarized recent progresses in transition metal oxide based electrode materials for supercapacitors. Different synthesis routes and electrochemical performances of electrode materials and storage mechanisms of supercapacitor devices have been presented in details. The future developing trends of supercapacitor based on metal oxide electrode materials are also proposed.

In past decades, increasing energy shortages have attracted wide attention of the scientists all over the world. To develop advanced energy storage devices with high energy density and power density has become new challenges [1–6]. Lithium (sodium) ion batteries have been widely studied due to their high energy density (30–200 Wh/kg). But they are often too bulky or rigid to be used for wearable or portable energy storage devices. Phase transformation usually can causes structural changes, which leads to low power density (~1 Wh/kg) and poor cycling life [7,8]. However, traditional supercapacitors as promising electrochemical devices have become research focuses for their long cycle life > 10,000 times, high power density ~10 Wh/kg and fast charge-discharge feature [9,10]. Based on the charge storage mechanism, supercapacitors can be divided into two types: electrical double-layer capacitors (EDLC) and pseudocapacitors [11–13]. EDLC stores electrical energy through an electrostatic accumulation of the charges in the interfaces of electric double-layers between electrode and electrolyte. Pseudocapacitors locate in between EDLC and battery. Their energy storage mechanism is a surface Faradaic electron transfer process of metal ions, which could be achieved by the insertion or adsorption of ions. But they usually present low energy density that restricts their practical applications [14–16]. Fig. 1 illustrates the schematic diagram of EDLC, pseudocapacitors and hybrid capacitors.

The earliest supercapacitor, EDLC, was found as an electrolytic capacitor in low voltage operation in 1957. After that, Stepanov *et al.* conducted the first investigation to combine the battery-type material of nickel oxide and capacitive carbon in one system, wherein the operating potential window of the device can be enlarged in an efficient manner and result in an enhanced energy density [17]. Later, more and more battery-type materials were introduced to assemble with capacitive materials as hybrid energy storage devices.

Pseudocapacitive electrode materials mainly conclude RuO_2 and MnO_2 electrode [18,19], which store charges through surface reactions of electrode materials. The charge transfer is merely restricted to the electrode/electrolyte interface within bulk material. Simultaneously, the structure of electrode material does not be destroyed during the charging/discharging process. However, battery type capacitors electrode materials present obvious redox peaks and the plateaus from CV and GCD curves, which demonstrate a diffusion-controlled electrochemical process with high energy density [20–24]. Electrochemical characteristics of EDLCs, pseudocapacitors and hybrid capacitors are shown in Fig. 2. Even so, it is still challenging to meet practical applications owning to the limited energy density that arises from low specific capacitance. An effective strategy is to fabricate hybrid capacitors, which make full use of the advantages both capacitor type electrode and battery type ones.

* Corresponding author.
E-mail address: wuxiang05@163.com (X. Wu).

https://doi.org/10.1016/j.cclet.2020.02.017

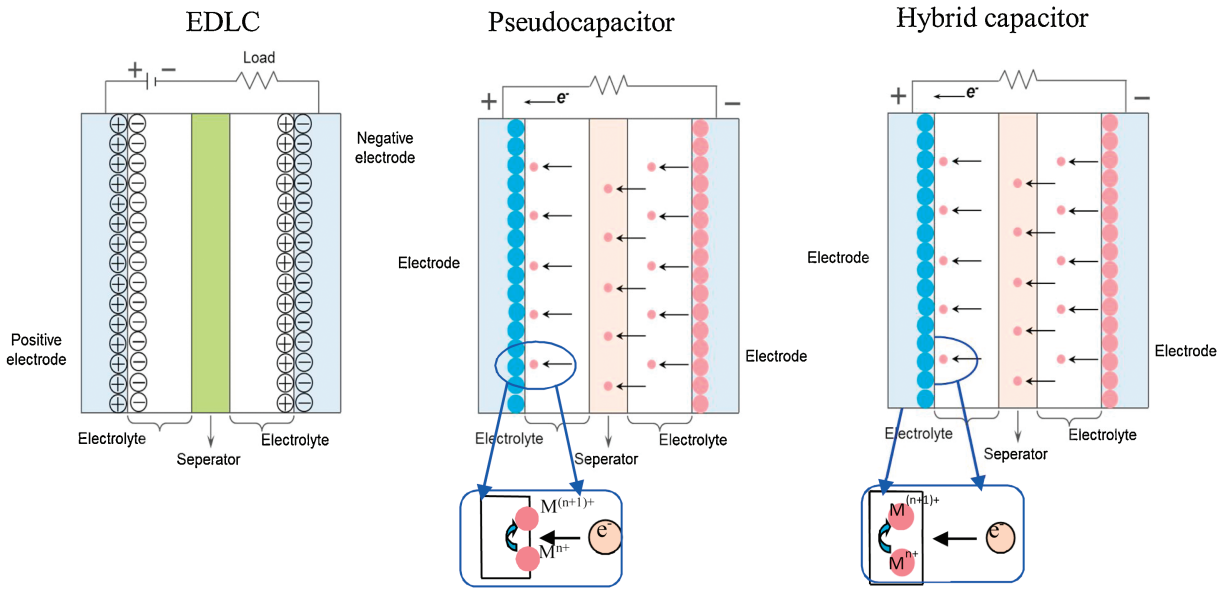

Fig. 1. Schematic diagram of EDLC, pseudocapacitor and hybrid capacitor.

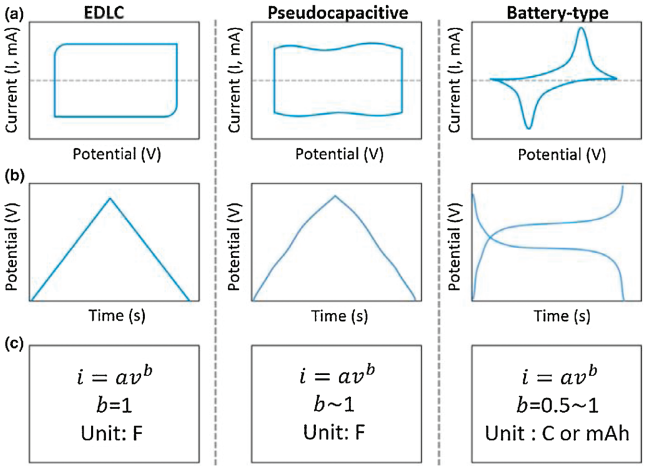

Fig. 2. Electrochemical characteristics of EDLC, pseudocapacitaor and hybrid capacitor. Reproduced with permission [23]. Copyright 2019, Wiley.

Based on above considerations, many efforts have been focused on developing novel electrode materials on nanoscale, which can deliver high energy and power density [25–28]. The active materials in the electroactive species contain hydroxides, transition metal oxides and conducting polymers [29–31]. High efficient energy storage devices require store large quantities of electrical energy in very small space and release them rapidly at the same time. Metal oxides have been research hotspots as potential electrode materials for hybrid capacitors due to their facile preparation methods, richness in nature and low cost, which benefits higher specific capacitance than EDLC electrode materials [32]. In addition, the size, morphology and crystal orientation of transition metal oxide can be easily regulated, which contributes comprehensive understanding the relationship of between electrode materials and electrochemical performance [33,34]. However, many metal oxide electrodes exhibit some disadvantages. For example, most of metal oxides present poor electrical conductivity [35], which causes some safe problem due to heat generation during long cycling stability, and leads to slow ion transport kinetics [36,37]. In order to address above issues, many efforts have been devoted to developing hybrid electrode materials. Herein, we summaries some advances in transition metal oxides as electrode materials for hybrid capacitors. These electrode materials include MnO_2, RuO_2, V_2O_5, WO_3, NiO, Co_3O_4, MCo_2O_4 and XMo_2O_4. Their morphologies, structures and electrochemical performance are investigated systematically.

1. Pseudocapacitive electrode materials

1.1. Manganese dioxide (MnO_2) electrode materials

Transition metal oxide manganese dioxide (MnO_2) has attracted widespread attention for its low cost, various crystal structures, environmental compatibility and high theoretical pseudocapacitance (1370 F/g) [38–40]. Thus far, varieties of wet-chemical and electrochemical methods have been developed to prepare nanostructured MnO_2 electrode materials [41,42]. However, the poor conductivity of MnO_2 (10^{-5}-10^{-6} S/m) leads to its low power and specific capacitance. In order to achieve high specific capacitance and excellent rate capability, it is vital to improve the electrical conductivity of MnO_2 electrode. Therefore, hybrid electrode structures are considered to increase the conductivity and charge-storage ability. Zhao *et al.* reported 3D MnO_2-graphene-CNT hybrid electrode with a specific capacitance of 377.1 F/g at 200 mV/s and 90% of its initial capacitance after 1000 cycles [43]. Yu *et al.* reported graphene oxide-MnO_2 nanocomposites with a capacitance of 370.7 F/g at 1 A/g and 99.3% capacitance retention after 5000 cycles [44]. Lu's group prepared TiO_2@MnO_2 heterostructured electrode with a capacitance of 139.6 F/g with excellent cycling stability [45]. However, these reported MnO_2 based electrode materials show either inferior specific capacity or relative poor cycling performance. Researchers concentrated on preparing other composites, such as MnO_2/C materials, including carbon nanofoam, carbon nanotubes and graphene. Unfortunately, carbon/MnO_2-based capacitors only show ideal capacitive behavior in aqueous electrolytes, where the potential window is relatively small, and consequently delivers limited energy and power densities [46]. To assemble asymmetric capacitor is considered to be a best way to solve this problem due to its combined different positive and negative electrode materials with well-separated potential windows.

The energy storage mechanism of MnO_2 electrode material is associated mainly with reversible redox reactions between

different oxidation states [47]. There are two mechanisms to explain the charge storage behavior, which contain the insertion of electrolyte cations ($C^+ = Li^+$, Na^+ and K^+) in the bulk of electrode and the surface adsorption of electrolyte cations on MnO_2 electrodes:

$$MnO_2 + C^+ + e^- \leftrightarrow MnOOC \quad (1)$$

$$(MnO_2)\ \text{surface} + C^+ + e^- \leftrightarrow (MnOOC)\ \text{surface} \quad (2)$$

MnO_2 nanosheet assembled porous nanotubes were fabricated through a hydrothermal process. The as-prepared nanotubes provide large surface area, which contributes effective contact from the electrolyte ions and affords short ion diffusion paths and fast kinetics. In addition, nanotube morphology can also accommodate large volume changes during the charge-discharge cycle and thereby improve the cycle stability of electrode [48]. A growth schematic of MnO_2 nanotubes was depicted in Fig. 3a. MnO_2 nanosheets were firstly fabricated and adsorbed on the surface of polycarbonate. As hydrothermal reaction further proceeds, Ostwald ripening process occurred, which smaller particles are consumed while the bigger ones grow into nanosheets with a lamellar structure. Subsequently, the nanosheets are assembled into porous MnO_2 nanotubes. Figs. 3b–d show SEM images of the samples. It is easily found that the average diameter of MnO_2 nanotubes is 200 nm, which is consistent with the average pore diameter of original polycarbonate (PC) membrane. The diameter and thickness of prepared MnO_2 nanotubes can be regulated by selection of membrane pore size. The as-prepared MnO_2 nanotubes exhibits a specific capacitance of 365 F/g at 0.25 A/g and capacitance retention of 90.4% after 3000 cycles. An asymmetric supercapacitor is assembled through porous MnO_2 nanotubes as positive electrode and graphene as negative electrode. The device delivers an energy density of 22.5 Wh/kg and a maximum power density of 146.2 kW/kg.

Zhao *et al.* reported MnO_2@$NiCo_2O_4$ core-shell structures through a simple synthesis method. The as-prepared products present a specific capacitance of 904.2 F/g at 1 A/g. The device delivers an energy density of 31.8 Wh/kg [49]. To further improve energy density of supercapacitors, Wang *et al.* developed low cost MnO_2 NWs and Fe_2O_3 NTs *via* a facile scalable method (Fig. 4). A solid-state flexible asymmetric supercapacitor was prepared with α-MnO_2 nanowires as positive electrode and amorphous Fe_2O_3 nanotubes as negative electrode. The as-assembled ASC device shows an energy density of 0.55 mWh/cm^3 and excellent rate capability [50].

Incorporating MnO_2 with other high electrical conductivity electrode materials has been investigated to extend the working

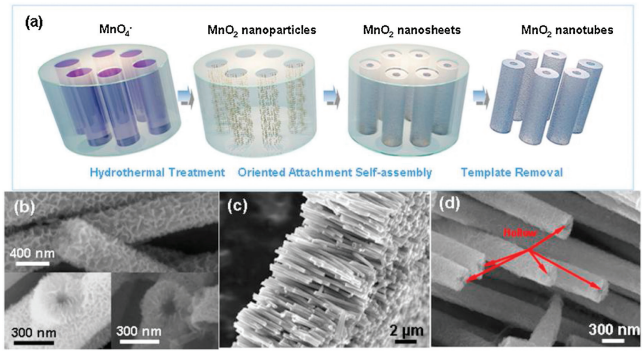

Fig. 3. (a) Schematic illustration of the synthesis procedure of porous MnO_2 nanotubes. (b) SEM images of MnO_2 nanotubes. (c) Side-view of MnO_2 nanotubes arrays. (d) Enlarged view of the MnO_2 nanotubes arrays. Reproduced with permission [48]. Copyright 2014, Nature group.

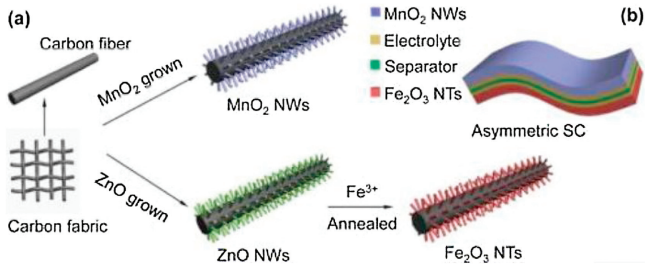

Fig. 4. (a) The synthesis procedure schematic of MnO_2 NWs and Fe_2O_3 NTs on carbon cloth. (b) Schematic sketch illustrating the designed asymmetric supercapacitor device. Reproduced with permission [50]. Copyright 2014, American Chemical Society.

voltage and improve the cycle stability. Liu's group reported wire-shaped asymmetric pseudocapacitors with both pseudocapacitive cathode and anode. Simultaneously, the device design with new cathode/anode coupling is proposed to achieve excellent electrochemical performance in a wire-type *quasi*-solid-state asymmetric pseudocapacitor (WQAP). The hierarchical α-MnO_2 nanorod@δ-MnO_2 nanosheet array cathode and MoO_2@C nanofilm anode are directly grown on flexible tiny Ti wires through hydrothermal and electrodeposition methods. The nanoarray/film electrode facilitates the integration with gel electrolyte of polyvinyl alcohol-LiCl. WQAP delivers high energy density and power density (9.53 mW h/cm^3 and 22,720 mW/cm^3, respectively), high voltage (2.0 V) and excellent cycle stability over 100000 times [51].

Zhao and co-workers synthesized MnO_2/GO composites through a facile chemical precipitation method. They used the as-synthesized product as the electrode materials for supercapacitor. Electrochemical measurements demonstrate that asymmetric supercapacitor presents a specific capacitance of 84 F/g at 0.1 A/g in 1 mol/L Na_2SO_4 solution and an energy density of 46.7 Wh/kg at a power density of 100 W/kg. In addition, the device exhibits superior long cycle life with 100% specific capacitance retention after 1000 cycles [52]. Cheng *et al.* prepared graphene/MnO_2 supercapacitor electrodes [53]. The prepared electrode demonstrates a specific capacitance of 328 F/g and power density of 25.8 kW/kg. Fan *et al.* reported high power and energy density ACS device based on graphene/MnO_2 and activated carbon nanofiber electrodes. The device delivers maximum energy density of 51.1 Wh/kg, which is much higher than that of MnO_2//DWNT cell (29.1 Wh/kg) [54].

1.2. Ruthenium oxide (RuO_2) electrode materials

RuO_2 has been considered as another candidate for pseudocapacitors owing to its high rate capability and excellent stability [55–58]. However, its poor cycling stability and expensive cost are a serious challenge [59]. Short lifetime may be associated with the charge storage mechanism of metal oxides. Repeatedly insertion and extraction of ions decreases the structural stability of electrode materials. Therefore, it is necessary to improve the cycle stability and reduce the cost of electrode materials. Lee and co-workers reported a solid-state ASC based on RuO_2 and graphene films [60]. A solid-state flexible ASC device was assembled through ionic liquid functionalized-chemically modified graphene (IL-CMG) film as a negative electrode and RuO_2-IL-CMG composite film as a positive electrode. As-fabricated device achieved a wide voltage range of 1.8 V, showing a specific capacitance of 175 F/g and energy (19.7 Wh/kg) at power densities of 6.8 kW/g. These are much higher than those of symmetrical SCs based on IL-CMG//IL-CMG assembly. Wang *et al.* reported a novel 3D hydrous RuO_2 nanoparticles anchored to graphene and CNT hybrid foam

(RGM) nanocomposite, which presents superior specific capacitance of 502.78 F/g and areal capacitance of 1.11 F/cm^2 [61].

2. Battery-type electrode materials

2.1. Vanadium pentoxide (V_2O_5) electrode materials

V_2O_5 is an intercalation compound for electrochemical energy storage owing to high capacitance, superior cycling stability and variable oxidation states [62–64]. However, its poor electrical conductivity, tendency to aggregate and high dissolution in liquid electrolyte affects the rate and cycling performance [65]. Engineering V_2O_5 into nanostructures has been considered an efficient method to overcome the limitation of poor electrical conductivity [66–68]. To improve its electronic conductivity, Zhu *et al*. developed an efficient approach for large-scale production of V_2O_5 nanosheets with a thickness of 4 nm. The as-prepared V_2O_5 structures show a specific surface area of 133 m^2/g and multilevel pores, which provide a large electroactive surface. In addition, the as-fabricated V_2O_5 electrode exhibits a specific capacitance of 451 F/g in Na_2SO_4 electrolyte and the capacitance retention is more than 90% after 4000 cycles [69]. Lu group's designed and fabricated hybrid structured CNT/V_2O_5 nanowires with a high specific capacitance >300 F/g at 1 A/g and excellent cycling stability. The asymmetric supercapacitors device based on CNT/V_2O_5 nanowire as positive electrode and active carbon as negative delivers an energy density of 40 Wh/kg at a power density of 210 W/kg [70]. Hetero-structures and hybrid structures have been recognized as an effective way to improve electrochemical performance of electrode materials due to the synergistic effects between different materials. Yolk-shelled V_2O_5 nanostructures composed of the ultrathin nanosheets were synthesized through a hydrothermal approach. As the electrode material, hybrid structured V_2O_5 electrode exhibits a specific capacitance of 704.17 F/g at 1.0 A/g and a capacity retention of 89% at 3.0 A/g after 4000 cycles. The device shows an energy density of 29.49 Wh/kg at power density of 800 W/kg, and 90.6% capacity retention after 2000 cycles. Simultaneously, two cells in series can easily light up the light-emitting diode (3 V) [71].

In order to solve the agglomeration problem of V-based materials, it is very important to construct three-dimensional (3D) network structure with high energy density and excellent cycle stability. Zhang *et al*. prepared ultra-thin hybrid structured reducing graphene oxide (rGO) and V_2O_5 nanostructures (Fig. 5). Well-crystallized V_2O_5 nanobelts can offer more electroactive sites and diffusion paths to enhance the pseudocapacitance, the layered structure of V_2O_5 nanobelts prevents rGO nanosheets from agglomeration and the large surface area of rGO nanosheets with superior electrical conductivity facilitates charge transport efficiently [72]. Benefiting from the unique structure, the rGO/V_2O_5 hybrid structure shows excellent electrochemical properties with a high specific capacitance of 310.1 F/g (1 A/g) and 195.2 F/g (10 A/g). The assembled symmetric supercapacitors based on hybrid structured rGO/V_2O_5 presents a gravimetric capacitance of 225.6 F/g at 0.5 A/g, energy density of 31.3 Wh/kg at power density of 249.7 W/kg and long cycle stability (90.2% after 5000 cycles).

In order to further improve the conductivity and electrochemical performance, V_2O_5/polyindole@activated carbon cloth (V_2O_5/PIn@ACC) materials are prepared through V_2O_5 nanostructures grown on activated carbon cloth (ACC) with an ion-exchange column. The introduction of PIn shell with close contact with V_2O_5 is beneficial for not only preventing V_2O_5 dissolution into the electrolyte by avoiding direct contact between them during cycling, but also affording a facile electron transport to ensure electrochemical activity. By matching V_2O_5/PIn@ACC with the negative electrode of reduced graphene oxide@activated carbon cloth (rGO@ACC), an asymmetric supercapacitors device was assembled, which obtained an energy density of 38.7 Wh/kg at a potential window of 1.8 V. Besides, the device shows capacitance retention of 91.1% after 5000 cycles [73].

2.2. Tungsten oxide (WO_3) electrode materials

WO_3 is a promising electrode material for energy storage applications owing to its various crystalline phase and oxidation states, high energy density, high volumetric capacitance and low cost [74–78]. However, its low electrical conductivity is a major shortcoming [79,80]. Wu's group prepared WO_3 nanotube bundles as the electrode materials through a template/surfactant-free hydrothermal process. As negative materials for supercapacitor, WO_3 nanotube bundles exhibits a specific capacitance of 615.7 F/g at 1 A/g and cyclic durability of 85.1% retention after 6000 cycles. The as-fabricated asymmetric supercapacitor presents an energy density of 80.1 Wh/kg at 3240 W/kg and excellent cycle stability [81]. To further improve electrochemical performance of electrode materials. Zhi *et al*. prepared h-WO_3 nanopillars with well-assigned structure through NaCl solution as a capping agent. The results show that WO_3 nanopillars present a specific capacitance of 421.8 F/g at 0.5 A/g [82]. Figs. 6a and b exhibit detailed analyses of the dominated energy storage mechanism, indicating that proton insertion dominates the electrochemical behavior of h-WO_3. The facile insertion of protons into h-WO_3 implies that crystal structure offers precise transport pathways. Evidently, the hexagonal crystal structure possesses large amount of tunnels: hexagonal tunnels along the [001] direction (Fig. 6a) and tetragonal tunnels formed by stacking of WO_6 octahedra

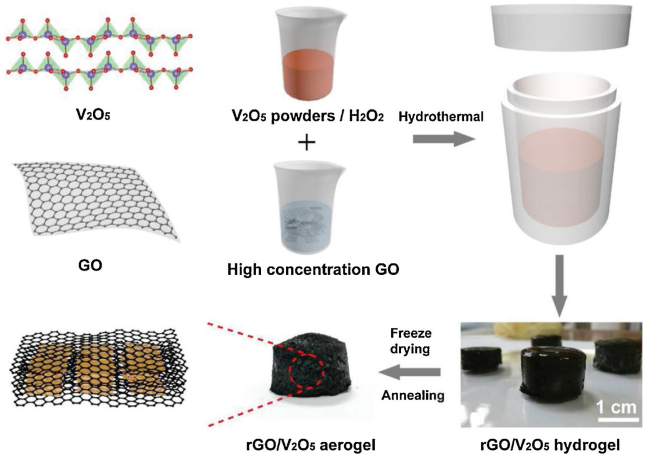

Fig. 5. Schematic illustrations for the synthetic process of rGO/V_2O_5 hybrid aerogels. Reproduced with permission [72]. Copyright 2019, Elsevier.

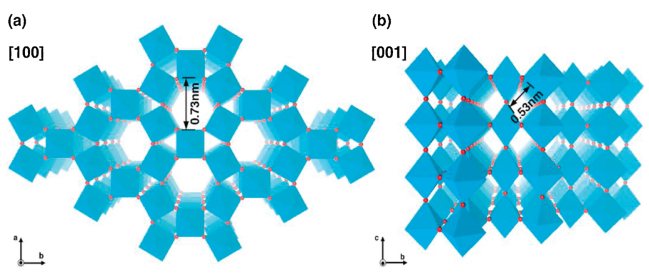

Fig. 6. Schemes of the hexagonal-phase tungsten oxides along the [001] and [100] directions of the microstructure of as-synthesized h-WO_3. Reproduced with permission [82]. Copyright 2014, American Chemical Society.

perpendicular to the [001] direction (Fig. 6b). The size and space of hexagonal tunnels are almost 5 times those of the tetragonal ones because the area of hexagonal tunnel is about 1.38 nm while the area of tetragonal one is only about 0.28 nm. Consequently, the effective proton insertion depth of hexagonal tunnels will be much larger than that of the tetragonal ones, resulting in its much high capacitance. In addition, integration of WO_3 with highly conducting materials such as carbon nanotubes (CNTs), carbon cloths, carbon fibers, conducting polymers, and graphene is recognized as one of the effective ways. He *et al*. fabricated WO_3@PPy nanowire arrays with a specific capacitance of 253 m F/cm^2 at 0.67 mA/cm^2 [83]. Nayak *et al*. prepared graphene-WO_3 nanowire nanocomposite with an optimized weight ratio, which shows an electrochemical performance with a specific capacitance of 465 F/g at 1 A/g and specific capacitance retention is 97.7% after 2000 cycles. The device exhibits an energy density of 26.7 Wh/kg at power density of 6 kW/kg [84].

2.3. Ferric oxide (Fe_2O_3) electrode materials

Hematite Fe_2O_3 is an alternative electrode material for ASCs due to its low cost, worldwide abundance, nontoxicity and high theoretical specific capacitance [85–88]. However, the intrinsically inferior electrical conductivity of Fe_2O_3 weakens its specific capacitance and power capability [89,90]. Some strategies have been taken to improve the specific capacitance of α-Fe_2O_3 materials, including tailoring the microstructure of the materials to shorten transfer path of ion and electrons, coating the surface with conductive polymers or carbon materials to improve the conductivity of the materials [91–93]. Zheng *et al*. fabricated α-Fe_2O_3 hierarchical structures supported on Ni foam for supercapacitor electrodes through a facile hydrothermal method, which presents an areal capacitance (681mF/cm^2 at 1 mA/cm^2) and long cycling stability (23.9% loss after 6000 cycles) [94]. Yu *et al*. reported a symmetric supercapacitor with high energy density (11.0 mWh/cm^3 at 1543.7 mW/cm^3) in 2.0 mol/L Li_2SO_4 aqueous solution. Hybrid electrode structure is considered to be an effective way to improve the cycle stability and specific capacitance of electrode material due to its unique structural characteristics [95]. Wu's group reported two kinds of hybrid α-Fe_2O_3@Co_3O_4 and α-Fe_2O_3@$MnCo_2O_4$ structures through simple solution method. The hybrid composites exhibit high capacitance and excellent cycling stabilities [96].

The stability of the device is a main indicator in evaluating its practical application. Guan *et al*. fabricated a hierarchical composite architecture of Fe_2O_3 nanoparticles, graphite foam and carbon nanotubes (GF-CNT@Fe_2O_3) with 111.2% capacitance retention after 50,000 cycles at 20 mA/cm^2 [97]. Dong *et al*. prepared a carbon-coated α-Fe_2O_3 (α-Fe_2O_3@C) core/shell nanowire arrays grown on a flexible carbon cloth by a simple hydrothermal method [98]. Wang *et al*. designed a thumb-ring-like α-Fe_2O_3/rGO electrode with a negative potential window of −1∼0.2 V, a specific capacitance of 255 F/g at 0.5 A/g and only about 10% decay after 11,000 cycles [99]. Xia *et al*. reported a novel strategy fabricated ultrafine Ni nanotube arrays with ultrathin tube walls through a modified template-assisted process (Fig. 7). The α-Fe_2O_3 nanoneedles are controlled electrodeposited on Ni nanotube arrays (NiNTAs@Fe_2O_3 nanoneedles) by a bottom-up strategy. The as-fabricated electrode materials show a specific capacitance of 418.7 F/g at 10 mV/s and a rate capability of 215.3 F/g at 64 A/g [100]. Li *et al*. prepared α-Fe_2O_3 nanowire arrays on carbon cloth by electrodeposition followed an annealed process. Then, 3D α-Fe_2O_3@PANI core-shell nanowire arrays are fabricated through electrodepositing a thin layer of PANI on α-Fe_2O_3 nanowires. Compared with single α-Fe_2O_3 electrode, hybrid structured α-Fe_2O_3@PANI electrode shows excellent electrochemical performance with twice increase in C_{sp} from 33.93 mF/cm^2 to 103 mF/cm^2. In addition, The device was assembled with α-Fe_2O_3@PANI nanowires grown on carbon as anode and PANI nanorods as cathode, which shows a volumetric capacitance of 2.02 mF/cm^3, an energy density of 0.35 mWh/cm^3 at a power density of 120.51 mW/cm^3, and excellent stability with specific capacitance retention of 95.77% after 10 000 cycles [101]. Lee *et al*. developed a facile approach to fabricate hybrid structured Fe_2O_3 NTs/reduced graphene oxide (rGO). The Fe_2O_3@rGO electrode presents a specific capacitance of 215 F/g at 2.5 mV/s, which is higher than single Fe_2O_3 electrode (30 F/g) [102]. Dong *et al*. fabricated spindle-like α-Fe_2O_3 and reduced graphene (rGO) composites through a simple hydrothermal method. The α-Fe_2O_3@rGO product exhibits high specific capacitance and cycle stability of 87.5% after 10,000 cycles. The ASCs device delivers an energy density of 73 Wh/kg at power density of 1357 W/kg, and 219% capacitance retention after 10,000 cycles (Fig. 8) [103].

Recently, doping and oxygen vacancy regulation of electrode materials have attracted much attention to improve total performance of the devices [104,105]. Ti^{4+} has been reported to be an electron donor through replacing Fe^{3+} and decreasing Fe^{3+} to Fe^{2+}. Core/shell structured Ti-Fe_2O_3@PEDOT electrode exhibits high specific capacitance of 1.15 F/cm^2 at 1 mA/cm^2. ASCs device demonstrates maximum energy density of 0.89 mW h/cm^3 and maximum power density of 0.44 W/cm^3, and a cycling durability with more than 96% capacitance retention after 30,000 cycles [106]. Sun *et al*. fabricated heterostructured oxygen-deficient $Fe_2O_{3-\delta}$ nanorod arrays with a unique crystalline core/amorphous shells. The crystalline/amorphous interface greatly improves charge storage sites for high specific capacitance. The device was assembled using the as-prepared Co_3O_4 nanosheet arrays as positive electrode and $Fe_2O_{3-\delta}$ nanorods arrays as negative one. It delivers an energy density of 0.33 mWh/cm^3 [107]. Hu *et al*. reported the hierarchical T-Fe_2O_3/polypyrrole (PPy) nanoarrays (NAs) by a self-sacrificing template methods. T-Fe_2O_3/PPy NAs electrode exhibits an areal specific capacitance of 382.4 mF/cm^2 at 0.5 mA/cm^2 and capacitance retention of 97.2% after 5000 cycles. ASC device delivers an energy density of 0.22 mWh/cm^3 at power density of 165.6 mW/cm^3 [108]. Liu's group fabricated thumb-ring-like α-Fe_2O_3@rGO hybrid structured electrode materials through a two-step hydrothermal procedure and a surfactant modification. Hybrid structured α-Fe_2O_3@rGO electrode exhibits a rate performance with 75% of capacitance retention with the scan rate from 5 mV/s to 200 mV/s and a cycling stability with about 10% decrease of the initial capacitance after 11,000 cycles [109].

2.4. Nickel oxide (NiO) electrode materials

NiO has been widely studied as a positive material due to its high electroactive nature, cost effectiveness, high theoretical specific capacitance of 2584 F/g [110–113]. Additionally, as transition metal oxide, NiO presents relatively higher electrical conductivity than other metal oxides/hydroxides or polymers [114–116]. However, the real specific capacitance of NiO nanomaterials is still far below the theoretical value [117]. Thus, it is important to develop a facile, environmentally friendly method to synthesize unique structured NiO electrode materials with high specific capacitance and excellent cycle stability. Lou *et al*. reported NiO nanobelts through a hydrothermal process, which presents superior electrochemical performance with a specific capacitance of 1126 F/g at 1 A/g, and 95% of the capacitance of the first capacitance were maintained after 2000 cycles [118]. Jang *et al*. prepared porous NiO nanostructures with different morphologies through a sol-gel method. The prepared NiO samples exhibit a specific capacitance of 480 F/g at 0.5 A/g [119]. O-vacancy enriched NiO hexagonal platelets have been fabricated by a facile

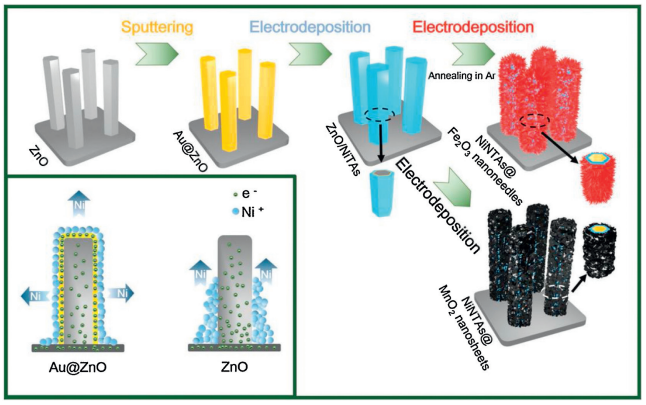

Fig. 7. Schematic illustration of the synthesis procedure for the NiNTAs@Fe_2O_3 nanoneedles and NiNTAs@MnO_2 nanosheets. The inset shows different Ni films formed on ZnO nanorod with and without Au layer. Reproduced with permission [100]. Copyright 2018, Wiley-VCH.

hydrothermal treatment in H_2O_2 aqueous solution [120]. Due to self-growing nature and abundant oxygen vacancies, the as-prepared NiO electrode shows a specific capacitance of 2495 F/g at 1 mV/s and the capacitance retention is higher than 80% with the current density increasing from 0.5 A/g to 10 A/g. Li's group reported hybrid structured NiO@rGO materials through a facile method. Based on large specific area and excellent conductivity of rGO, the asymmetric supercapacitor device shows an operating voltage of 1.7 V and an areal capacitance of 248 mF/cm^2 at 1 mA/cm^2, energy density of 39.9 Wh/kg [121]. To further improve specific capacitance of NiO-based electrode materials, Feng *et al.* designed vertically standing structured graphene@NiO nanosheet arrays electrode (Fig. 9). The prepared NiO nanosheets were converted into nanoscale NiO particles encapsulated in graphene layers through plasma chemical vapor deposition process. The hetero-structured graphene@NiO product presents specific capacitance of 2146 F/g [122]. It is been generally believed that the electrochemical performance of NiO nanostructure largely depends on its morphology, surface area and the presence of dopants [123–125]. Cao *et al.* used a template-free microwave-assisted gas/liquid interfacial method to synthesize flowerlike NiO hollow nanospheres. The prepared samples show excellent electrochemical properties with specific capacitance of 585 F/g at 5 A/g and excellent cycling performance [126]. Hu and his coworkers reported three-dimensional nanoporous NiO film through an electrochemical route. The as-prepared NiO film shows highly porous structure with surface area of 264 m^2/g. The results showed the electrode materials deliver a specific capacitance of 1776 F/g [127].

2.5. Cobalt oxide (Co_3O_4) electrode materials

Co_3O_4 has received a considerable attention as the electrode material due to its excellent electrochemical performance, high theoretical specific capacitance, environment benign and morphological diversity [128–132]. The capacitive reactions of Co_3O_4 electrode can be described as follows [133]:

$$CoO + OH^- + H_2O \rightarrow 3CoOOH + e^- \quad (3)$$

$$CoOOH + OH^- \rightarrow CoO_2 + H_2O + e^- \quad (4)$$

To obtain large specific capacitance, Co_3O_4 nanostructures with various morphologies have been prepared. Co_3O_4 nanoflakes could be grown on nickel foam through a simple one-step hydrothermal route. The as-synthesized products showed a capacitance of 518 mF/cm^2 at 1 mA/cm^2 and 75% capacitance retention after 6000 cycles [134]. However, Co_3O_4 material possesses poor electrode stability and low specific capacity, which limit their practical

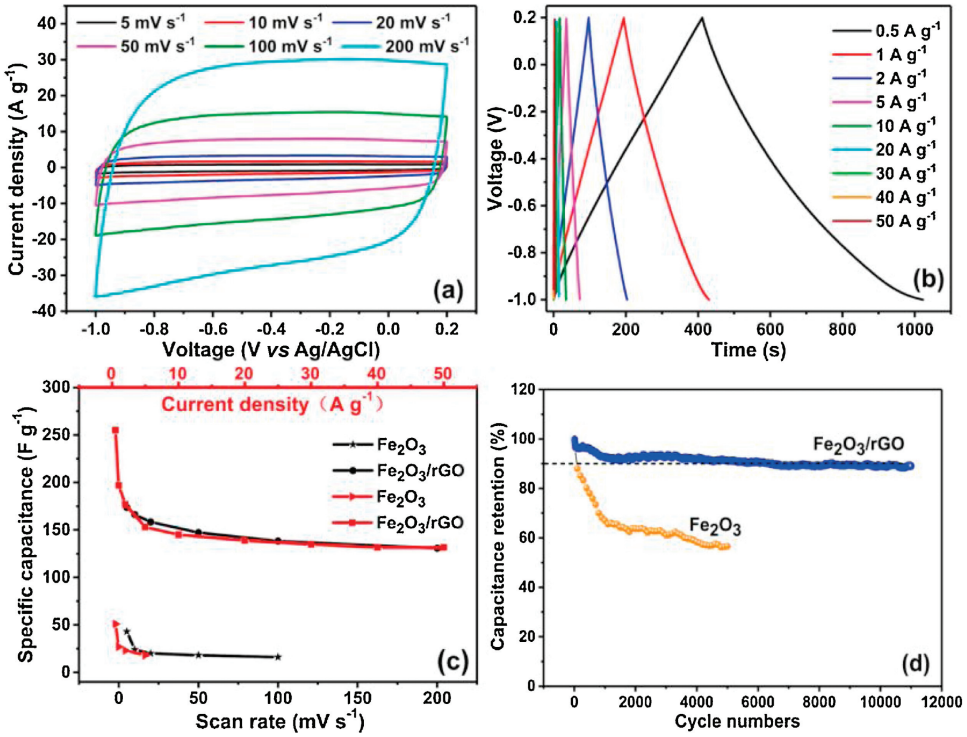

Fig. 8. Electrochemical performance of the activated α-Fe_2O_3/rGO electrode: (a) CV and (b) GCD curves. (c) Specific capacitances and (d) cycle performance at 10 A/g. Reproduced with permission [103]. Copyright 2018, Elsevier.

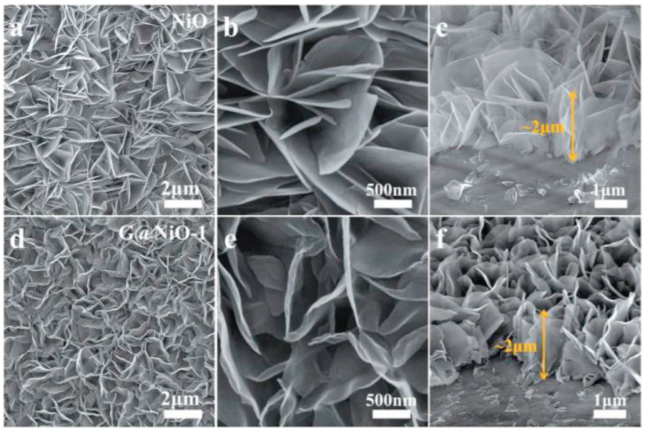

Fig. 9. SEM images of the as-prepared products (a-c) NiO and (d-f) G@NiO nanosheet arrays. Reproduced with permission [122]. Copyright 2018, Wiley.

applications. Simultaneously, large volume expansion/contraction is related to alkali ion insertion and extraction process, leading to electrode material shed, large capacity loss and poor cycle stability [135]. Thus, to improve the electrochemical performance of electrode, the combination of two metal oxide nanomaterials presents better electrochemical performances. Recently, Zheng *et al.* prepared 3D Co_3O_4@MnO_2 heterostructures on Ni foam through a facile hydrothermal method. Co_3O_4 products with high specific area were acted as the scaffolds to support MnO_2 samples. Hybrid structured Co_3O_4@MnO_2 electrode exhibits an initial discharge capacitance of 1397.2 mF/cm^2 at 1 mA/cm^2. After 6000 cycles, the hybrid structure can maintain its discharge capacitance of 86.1% (Fig. 10) [136]. Shen and his co-workers fabricated nanowires-assembled Co_3O_4@$NiCo_2O_4$ architectures through two-step hydrothermal process. Owing to the synergistic effect between Co_3O_4 scaffolds and $NiCo_2O_4$ nanowires, hybrid Co_3O_4@-$NiCo_2O_4$ structure exhibits an areal specific capacitance of 9.12 F/cm^2 at 2 mA/cm^2. The device presents a maximum voltage of 1.0 V with an areal specific capacitance of 1343.7 mF/cm^2 at 2 mA/cm^2. No obvious capacitance attenuation appears after 5000 cycles at the current density of 10 mA/cm^2 [137]. Wu's group reported Co_3O_4@$NiCo_2O_4$ core-shell structures fabricated on flexible carbon cloth using a facile hydrothermal method (Fig. 11). The as-fabricated core-shell structures show an areal capacitance of 4.35 F/cm^2 at 1 mA/cm^2 and specific capacitance of 1450 F/g at 1 A/g and excellent cycle stability (~4.2% loss after 6000 cycles). They attributed the enhanced electrochemical behaviors to rational design of $NiCo_2O_4$ nanoflakes adhering on Co_3O_4 nanowires, which promotes two electroactive materials utilizing the synergistic effect to supply more pathways for accelerating fast electron and ion transfer [138].

3D Co_3O_4 nanowires@NiO nanosheet arrays were synthesized using a simple hydrothermal method [139]. The electrochemical results demonstrate that the specific capacitances reach 2018 mF/cm^2 (at 2 mA/cm^2) and 608 F/g (2 A/g). An asymmetric supercapacitor was assembled with Co_3O_4 nanowire@NiO nanosheet as positive electrode and activated carbon (AC) as negative electrode, revealing capacity retention rate of 73.5% after 10,000 cycle. In additon, many cobalt oxide/hydroxide nanomaterials have been reported [140–142]. Pang *et al.* developed a controllable one-pot hydrothermal methodology to prepare heterogeneous Co_3O_4 nanocube/$Co(OH)_2$ nanosheet hybrids. The as-assembled device using the hybrid structured electrodes delivers the maximum energy density of 9.4 mWh/cm^3 with excellent cycle stability after 5000 cycles [143]. The two-dimensional core-shell architecture exposes numerous active sites for fast faradic reaction, resulting in increased reaction sites and a close contact of the electrolyte with the shell. An assembled supercapacitor shows a specific capacitance of 98.4 F/g at 5 mA/cm^2 and high energy density of 40.0 Wh/kg at a power density of 349.6 W/g [144].

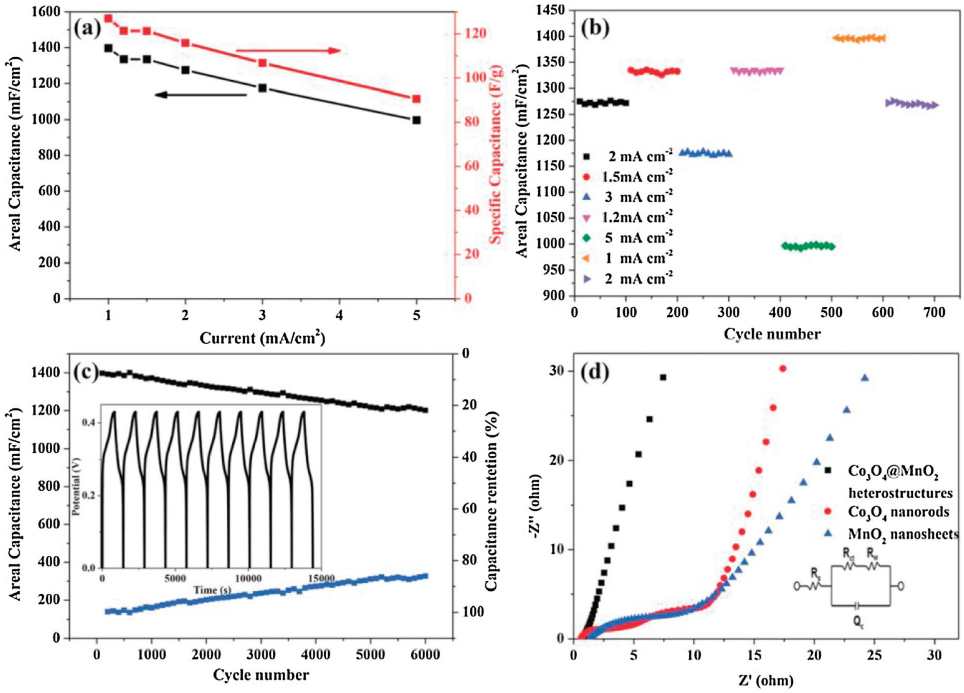

Fig. 10. Electrochemical performance of hybrid structured electrode materials. (a) Areal capacitance and specific capacitance. (b) Current density dependent cycling performance. (c) Cycling stability. (d) Nyquist plots. Reproduced with permission [136]. Copyright 2018, Royal Society of Chemistry.

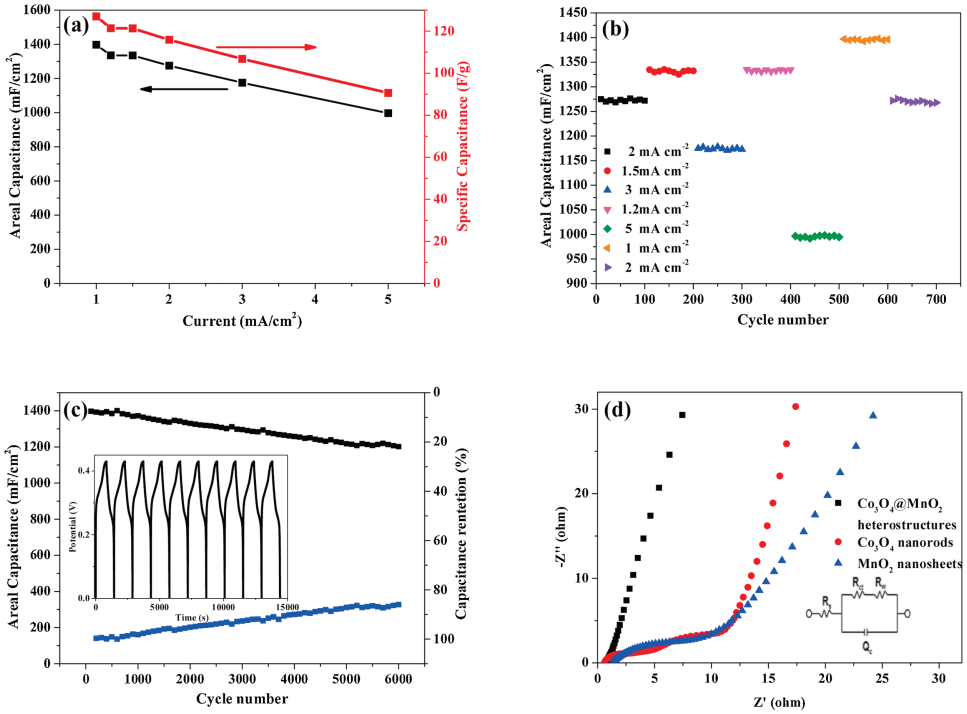

Fig. 11. Electrochemical performances of the as-prepared samples. (a) Areal capacitance and corresponding specific capacitance. (b) Cycling performance. (c) Cycling performance and capacitance retention of 3D Co_3O_4@MnO_2 heterostructures. (d) Nyquist plots, the inset is the AC impedance equivalent matching circuit diagram. Reproduced with permission [138]. Copyright 2018, Elsevier.

2.6. MCo_2O_4 (Ni, Zn, Fe) electrode materials

As ternary transition metal oxide, MCo_2O_4 with spinel structure presents much higher electrochemical activity and better electrical conductivity than those of single oxides [145–147]. In addition, MCo_2O_4 nanomaterials show different shapes and orientations [148,149]. The redox peaks of electrode materials can be ascribed to the faradaic effect. The corresponding redox reactions are illustrated as follows [150,151]:

$$MCo_2O_4 + H_2O + OH^- \leftrightarrow MOOH + 2CoOOH + e^- \quad (5)$$

$$2CoOOH + OH^- \leftrightarrow 2CoO_2 + H_2O + e^- \quad (6)$$

Lou *et al.* fabricated hierarchical $NiCo_2O_4$ tetragonal microtubes through using annealing nickel cobalt layered double hydroxide microtubes. The unique structural features can accelerate the transfer of electrons. The prepared sample exhibits an excellent electrochemical performance in terms of high specific capacitance and superior cycle life [152]. Fig. 12 shows SEM images and structures of $NiCo_2O_4$ microtubes. Wang's group reported $NiCo_2O_4$ arrays with a capacitance of 1055.3 F/g at 1.0 A/g [153]. Wu *et al.* prepared mesoporous $NiCo_2O_4$ nanoneedle arrays grown on nickel foam through a facile hydrothermal method. $NiCo_2O_4$ nanoneedle exhibits an areal capacity of 1996 mF/cm^2 at 2 mA/cm^2, and 19.3% capacitance loss of initial capacitance after 12,000 cycles at 20 mA/cm^2. An assembled device using $NiCo_2O_4$ electrode as positive electrode delivers a volumetric energy density of 0.33 mWh/cm^3 at power density of 12 mWh/cm^3, and 140.6% capacitance is maintained after 8000 cycles [154]. Li *et al.* fabricated porous $ZnCo_2O_4$ nanostructures *via* a facile hydrothermal route. The result shows that morphology of electrode material can be adjusted from nanowire to nanobelt by changing reaction temperature. The prepared $ZnCo_2O_4$ nanostructures exhibit a specific capacitance of 776.2 F/g at 1 A/g and excellent cycle stability [155]. Shen *et al.* synthesized hierarchical $ZnCo_2O_4$/nickel foam architectures through hydrothermal methods. Electrochemical measurements demonstrate that $ZnCo_2O_4$ electrode possesses the specific capacitance of 1400 F/g at 1 A/g, excellent rate capability (72.5% capacity retention at 20 A/g), and cycling stability (only 3% loss after 1000 cycles at 6 A/g) [156]. Zhang *et al.* fabricated mesoporous $NiCo_2O_4$ nanowire arrays through a simple surfactant-assisted hydrothermal method. The as-prepared mesoporous $NiCo_2O_4$ nanowires consist of numerous highly crystalline nanoparticles. From Fig. 13a, it can be found that the average diameter of $NiCo_2O_4$ nanowires is 150 nm. A high magnification TEM image is depicted in Fig. 13b, which further reveals that $NiCo_2O_4$ nanowire is composed of many nanoparticles. A lattice spacing of 0.47 nm is found in Fig. 13c, which is consistent with the theoretical inter-plane spacing of spinel $NiCo_2O_4$ (111) planes. SAED pattern (Fig. 13d) shows well-defined diffraction rings, which correspond to the (440), (224), (311), (111), (220) and (400) planes of $NiCo_2O_4$ structures, indicating that $NiCo_2O_4$ nanowire possesses polycrystalline structure [157]. However, the crystalline MCo_2O_4 electrode materials often expand or shrink significantly during charge-discharge process due to its high amount of charge storage. Combination of two or more electrode materials has been considered to be an effective method, which can further show the synergistic effect between active materials [158]. Based on the influence of conductivity on the electrochemical properties of electrode materials, the core-shell structured electrode materials have prepared through coating a layer of nanomaterials with better conductivity on the surface of MCo_2O_4 electrode materials [159]. Zhang *et al.* prepared $ZnCo_2O_4$@MnO_2 nanotube arrays electrode by a facile two-step method (Fig. 14) [160]. Heterostructured $ZnCo_2O_4$@MnO_2 nanotube presents a specific capacitance of 1981 F/g (2.38 F/cm^2) at 5 A/g and cycling stability (5000 cycles). The device with an operating voltage window of 1.3 V delivers a specific capacitance of 161 F/g at 2.5 mA/cm^2 with a maximum energy density of 37.8 Wh/kg and a capacitance retention of 91%

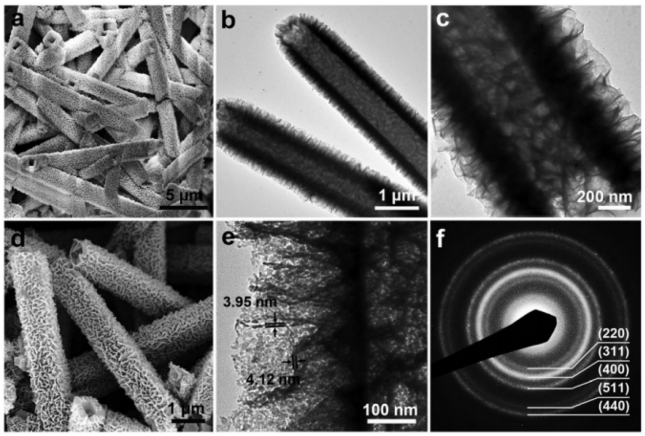

Fig. 12. NiCo-LDH tetragonal microtubes synthesized at 160 °C for 12 h. (a) FESEM images, (b, c) TEM images, (d) FESEM, (e) TEM image, (f) SAED pattern of as-prepared hierarchical $NiCo_2O_4$ microtubes. Reproduced with permission [152]. Copyright 2016, Royal Society of Chemistry.

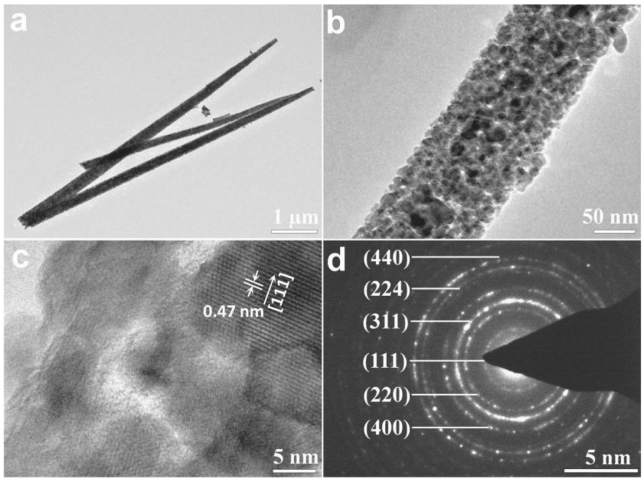

Fig. 13. Morphology and structure characteristic of $NiCo_2O_4$ naowires. (a, b) TEM; (c) HRTEM images; (d) SAED pattern. Reproduced with permission [157]. Copyright 2014, Wiley-VCH.

after 5000 cycles. Ternary MCo_2S_4 material exhibits about 100 times higher conductivity than the corresponding mixed oxide counterparts due to their rich redox reactions and synergistic effects of two metal ions [161]. Therefore, mixed metal sulfides could be utilized as alternative electrode materials for hybrid capacitors. Shao *et al.* reported the mesoporous polyhedron-structured NCO and NCS nanoparticles through molecular design of Ni and Co bimetallic ZIFs as solid precursors. The prepared products show high specific capacitance of 1296 F/g at 1 A/g. The device exhibits high energy density of 44.8 Wh/kg at 794.5 W/kg [162].

Compared to carbon based supercapacitors, pseudocapacitors show much higher capacitance. However, the Faradaic reactions typically are much slower in rate than ion adsorption over carbon surfaces. Thus, the rate capability is a big concern for the development of pseudocapacitance. Due to its high porosity, large internal surface area, and superior electrical and mechanical performance, three dimensional graphene networks (3DGNs) are used to strike platform for construction of composite electrodes with increased electrochemical performance [163]. Zhang *et al.* prepared $NiCo_2O_4$ nanosheet-coated three dimensional graphene networks with high-rate ability and long cycle-life. The novel $NiCo_2O_4$ NS/3DGN hybrid structure exhibits ultrahigh specific capacitances as well as excellent rate capability of 2173 and 954 F/g at high current densities of 6 and 200 A/g, respectively. Especially, it shows superior cycle stability with only 6% capacitance loss after 14,000 cycles at 100 A/g [164].

In addition, polymer polypyrrole (PPy) with higher electrical conductivity (10–100 S/cm) than oxides and sulfides, has also been widely investigated. Lu and his coworkers fabricated heterogeneous $NiCo_2O_4$@polypyrrole core/sheath nanowire arrays on Ni foam with an areal capacitance of 3.49 F/cm^2 at 5 mA/cm^2, which is almost 1.5 times as much as single $NiCo_2O_4$ (2.30 F/cm^2). Moreover, it can remain 3.31 F/cm^2 (94.8% retention) after 5000 cycles. It is generally believed that the interfaces of electrode materials show abundant active sites and quick charge transfer efficiency [165]. Wu group's reported bi-interface induced multi-active MCo_2O_4@MCo_2S_4@PPy (M = Ni, Zn) sandwich structure through a facile prepare process. The as-prepared products are acted directly as the electrode materials for hybrid capacitors. The MCo_2O_4@MCo_2S_4@PPy-24 electrode shows specific capacitance of 835.2 C/g at 1 A/g and capacitance retention of 90.07% after cycles of 10,000 times. The ASC device was assembled based on MCo_2O_4@MCo_2S_4@PPy-24 as positive electrode and AC as negative electrode. It presents an energy density of 23.75 Wh/kg at power density of 5945.1 W/kg (Fig. 15) [166].

2.7. XMo_2O_4 electrode materials

Transition metal oxides, typically ternary metal oxides with two different metal cations, have been considered as advanced electrodes materials because of their improved redox reactions and excellent electrical conductivity [167,168]. Among various oxides, ternary metal molybdates, such as $MnMoO_4$, $CoMoO_4$ and $NiMoO_4$, have received increasing interest [169–171]. Although different morphologies of $CoMoO_4$ structures, including bundle-like structures and sheets, have been developed, the practical application of $CoMoO_4$ electrodes in ASCs is still hindered by their poor conductivity. Therefore, the controllable fabrication of $CoMoO_4$ electrode materials with desirable micro-/nanostructures is imperative.

It is well confirmed that hierarchical nanostructures assembled from low-dimensional building blocks such as 2D nanosheets and1D nanorods, have been considered as promising structures in the field of energy storage [172–175]. Yu and his coworkers presented a cost-effective, simple, and industry compatible strategy for the growth of honeycomb-like (NHC) $CoMoO_4$ strongly coupled on 3D graphene foam (Fig. 16). $CoMoO_4$-3D graphene hybrid (NSCGH) as electrode materials shows excellent specific capacitance as high as 2741 F/g at current density of 1.43 A/g. The as-fabricated hybrid structure maintains its initial capacitance of 96.36% after 100000 cycles. The as-fabricated device delivers a high energy density of 21.1 Wh/kg at a power density of 300 W/kg. With charge/discharge cycling up to 10000 times, the asymmetric supercapacitor still remained 87.42% of its initial specific capacitance [176].

3. Conclusions and outlook

Hybrid supercapacitor is a key to bridge the gap between conventional metal ion batteries and supercapacitors. We have summarized recent development in design and fabrication of transition metal oxide based electrode materials for hybrid capacitors. It is very important to integrate active/synergistic nanostructures into flexible substrates to improve energy density and power density of the devices. Moreover, integrating diverse conducting agents can also improve the overall electrical conductivity of metal oxide films/arrays. It is desired to

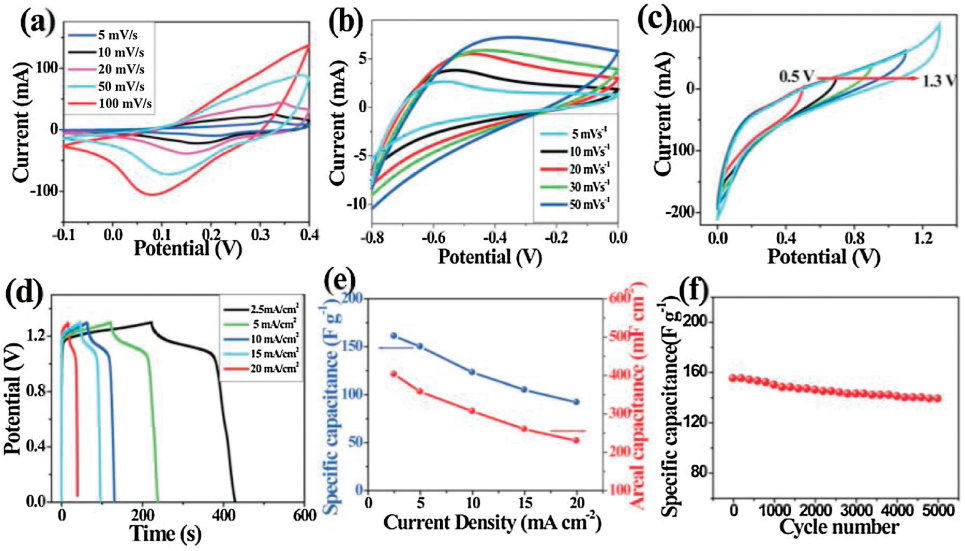

Fig. 14. Electrochemical performances of $ZnCo_2O_4$@MnO_2 NTs arrays and α-Fe_2O_3 electrodes. (a) CV curves. (b) CV curves at different scan rates. (c) CV curves of the assembled ASC device. (d) GCD curves of ASC device. (e) Specific capacitances of as-designed $ZnCo_2O_4$@MnO_2//α-Fe_2O_3-ASC device. (f) Cycle performance of the $ZnCo_2O_4$@MnO_2//α-Fe_2O_3-ASC device at 5 mA/cm^2. Reproduced with permission [160]. Copyright 2018, American Chemical Society.

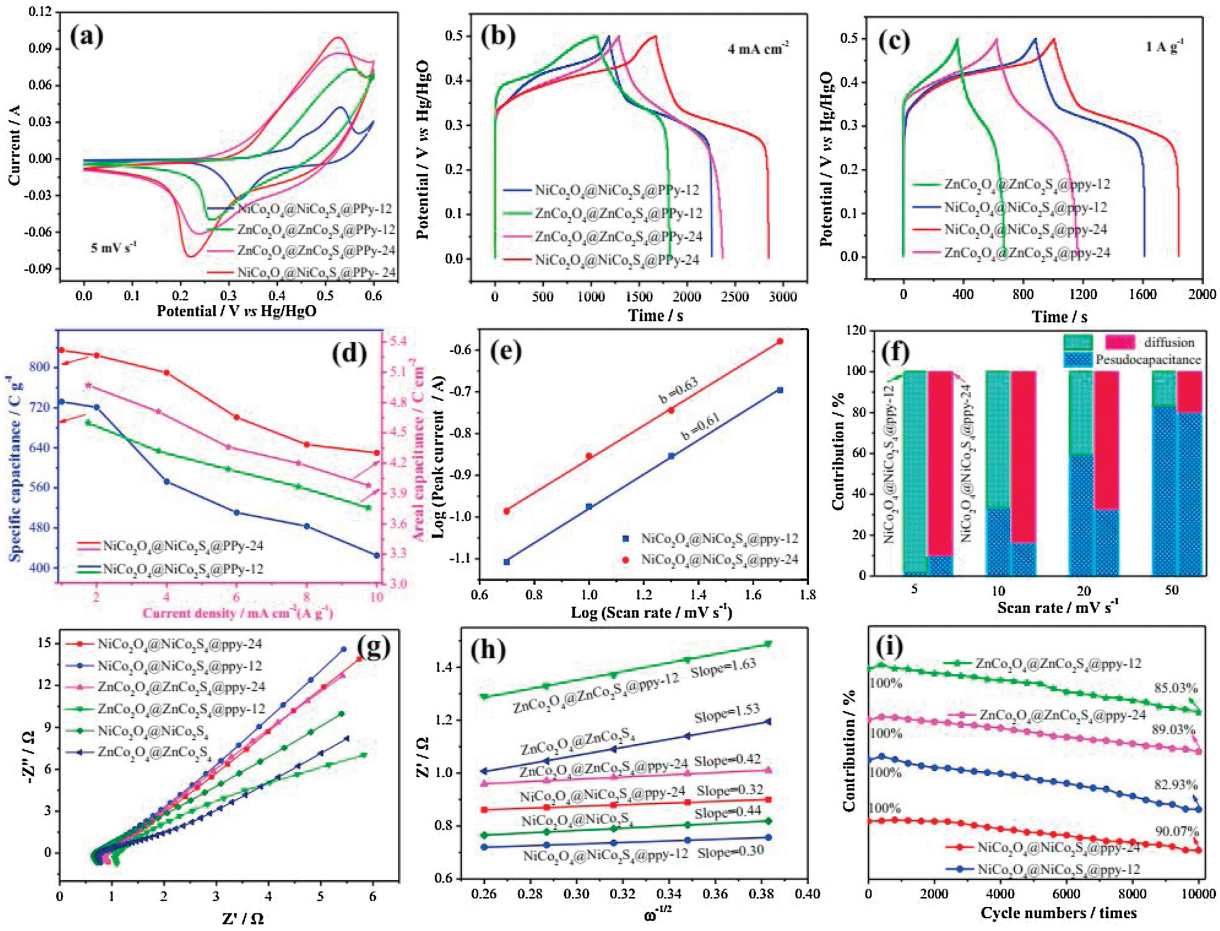

Fig. 15. Electrochemical performance of the as-prepared electrodes. (a) CV curves at 5 mV/s. (b) Charge-discharge curves at 4 mA/cm^2. (c) GCD curves at 1 A/g. (d) Specific and areal capacitances at different current densities. (e) b values of electrode materials at different scan rates. (f) Contribution ratio between capacitive capacities and diffusion-limited ones. (g) Nyquist plots. (h) Z' as a function of $\omega^{-1/2}$ plot in low frequency. (i) Cycling stability. Reproduced with permission [166]. Copyright 2018, Elsevier.

understand the electrochemical mechanisms of transition metal oxide-based hybrid electrodes and to investigate the physical/chemical properties of the interface within hybrid structures and their effects on the electrochemical performance. Although a lot of promising results have been achieved about transition metal oxide based electrode materials, low energy density is still a major problem for hybrid capacitors. In order to increase the energy density of electrode materials, the following aspects

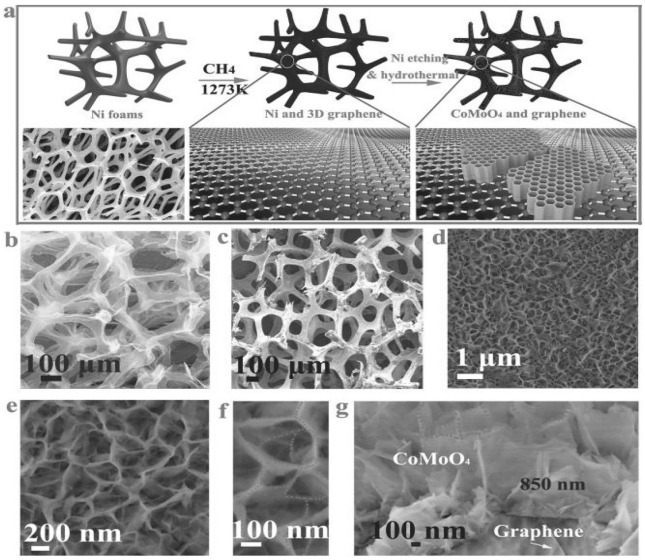

Fig. 16. (a) The typical synthesis procedure of honeycomb NHC-like $CoMoO_4$-3D graphene hybrid electrodes. (b) SEM images of 3D graphene. (c-f) SEM images of NHC-like strongly coupled $CoMoO_4$-3D graphene. (g) Cross-section SEM image. Reproduced with permission [176]. Copyright 2014, Wiley.

might be concerned: electron transfer kinetics can be improved through composing with high conductivity materials and heteroatom doping. Compared with Li-ion batteries, hybrid capacitors can delivers an energy density range from 10 Wh/kg to 100 Wh/kg, It is possible to be used on large scale in next generation energy storage system. However, significant efforts should be made to improve voltage window of hybrid capacitors. The development of novel electrode materials with unique architectures is required to obtain large surface area, fast electron transmission. Based on the synergistic effects, the combination of different electrode materials should be considered an efficient approach to enhance specific surface area and large potential window. In addition, it is important to further optimize the positive and negative electrode matching for the improvement of the device performance.

Declaration of competing interest

The authors declare no conflict of interest.

Acknowledgments

This work was supported by Education Department Funding of Liaoning Province (No. LJGD2019001), Guangxi Key Laboratory of Information Materials, Guilin University of Electronic Technology (No. 191010-K) and Guangxi Key Laboratory of Electrochemical Energy Materials (No. 2019001).

References

[1] F. Bonaccorso, L. Colombo, G. Yu, et al., Science 347 (2015) 1246501.
[2] Y. Gogotsi, P. Simon, Science 334 (2011) 917–918.
[3] X. Xiao, H.B. Song, S.Z. Lin, et al., Nat. Commun. 7 (2016) 11296.
[4] M.R. Lukatskaya, B. Dunn, Y. Gogotsi, Nat. Commun. 7 (2016) 12647–12659.
[5] P. Simon, Y. Gogotsi, B. Dunn, Science 343 (2014) 1210.
[6] W.H. Zuo, R.Z. Li, C. Zhou, et al., Adv. Sci. 4 (2017) 1600539.
[7] Y. Zhao, S. Huang, M. Xia, et al., Nano Energy 28 (2016) 346–355.
[8] J.Y. Huang, M. Zhong, F.K. Shi, et al., Angew. Chem. Int. Ed. 56 (2017) 9141–9145.
[9] P. Wu, S. Cheng, M.H. Yao, et al., Adv. Funct. Mater. 27 (2017) 1702160.
[10] W.W. Liu, M.H. Zhu, J.H. Liu, X. Li, J. Liu, Chin. Chem. Lett. 30 (2019) 750–756.
[11] J. Yan, Q. Wang, T. Wei, Z.J. Fan, Adv. Energy Mater. 4 (2014) 1300816.
[12] L.N. Gao, X.F. Wang, Z. Xie, et al., J. Mater. Chem. A 1 (2013) 7167–7173.
[13] P. Wang, C.Y. Li, W.G. Wang, et al., Chin. Chem. Lett. 29 (2018) 612–615.
[14] Y. Liu, Y. Jiao, B.S. Yin, et al., J. Mater. Chem. A. 3 (2015) 3676–3682.
[15] Z.F. Zhao, X.J. Wang, M.J. Yao, et al., Chin. Chem. Lett. 30 (2019) 915–918.
[16] C. Wang, J. Wang, X. Xiao, et al., Chin. Chem. Lett. 30 (2019) 1269–1272.
[17] A. B. Stepanov, I. N. Varakin, V. V. Menukhov, US Patent, US5986876A, 1999.
[18] C. Liu, X. Wu, Mater. Res. Bull. 103 (2018) 55–62.
[19] Z.K. Peng, X. Liu, H. Meng, et al., ACS Appl. Mater. Interfaces 9 (2017) 4577.
[20] J.M. Tarascon, M. Armand, Nature 414 (2001) 359.
[21] C.C. Zhuang, L. Li, Y. Liu, C.C. Ban, X.W. Liu, Chin. Chem. Lett. 29 (2019) 954–958.
[22] A. Manthiram, J. Phys, Chem. Lett. 2 (2011) 176.
[23] Y.Q. Li, J.P. Liu, Energy Environ, Mat. 2 (2019) 30.
[24] M.R. Lukatskaya, B. Dunn, Y. Gogotsi, Nat. Commun. 7 (2016) 12647.
[25] V. Augustyn, P. Simon, B. Dunn, Energy Environ. Sci. 7 (2014) 1597.
[26] H.Q. Liu, D.P. Zhao, P.F. Hu, X. Wu, Chin. Chem. Lett. 29 (2018) 1799–1803.
[27] D. Tie, S.F. Huang, J. Wang, et al., Energy Storage Mater. 21 (2019) 22–40.
[28] Y. Zhao, J.F. He, M.Z. Dai, et al., J. Energy Chem. 45 (2020) 67–73.
[29] Y. Liu, Y. Jiao, Z.L. Zhang, et al., ACS Appl. Mater. Interfaces 6 (2014) 2174–2184.
[30] X.Y. Zhang, S.J. Deng, Y.X. Zeng, et al., Adv. Funct. Mater. 28 (2018) 1805618.
[31] Y. Chen, G.Z. Chen, Acta Phys. Chem. Sin. 36 (2020) 1904025.
[32] J. Liu, M. Zheng, X. Shi, H. Zeng, H. Xia, Adv. Funct. Mater. 26 (2016) 919–930.
[33] M.C. Liu, L.B. Kong, C. Lu, et al., ACS Appl. Mater. Interfaces 4 (2012) 4631–4636.
[34] Y. Liu, P.F. Hu, H.Q. Liu, et al., Inorg. Chem. Front. 6 (2019) 2824–2831.
[35] K. Wang, Q.H. Meng, Y.J. Zhang, Z.X. Wei, M.H. Miao, Adv. Mater. 25 (2013) 1494–1498.
[36] M.R. Lukatskaya, S. Kota, Z.F. Lin, et al., Nat. Energy 2 (2017) 17105.
[37] Y. Liu, D.P. Zhao, H.Q. Liu, A. Umar, X. Wu, Chin. Chem. Lett. 30 (2019) 1105–1110.
[38] B.S. Yin, S.W. Zhang, Y. Liu, et al., CrystEngComm 16 (2014) 9999–10005.
[39] Y. Zhao, M.Z. Dai, D.P. Zhao, et al., CrystEngComm 21 (2019) 3349–3355.
[40] S. Lee, G. Nam, J. Sun, et al., Angew. Chem. 55 (2016) 8599–8604.
[41] D.P. Zhao, X. Wu, C.F. Guo, Inorg. Chem. Front. 5 (2018) 1378–1385.
[42] H. Jiang, C.Z. Li, T. Sun, J. Ma, Nanoscale 4 (2012) 807–812.
[43] T.K. Zhao, S.S. Guo, Y.X. Zhao, et al., Fuller. Nanotube Car. N. 5 (2015) 391–396.
[44] H.P. Yang, J. Jiang, W.W. Zhou, et al., Nanoscale Res. Lett. 6 (2011) 531–538.
[45] X. Lu, M. Yu, G. Wang, et al., Adv. Mater. 25 (2013) 267–272.
[46] J.G. Wang, Y. Yang, Z.H. Huang, F.Y. Kang, Carbon 6 (2013) 190–199.
[47] B. Messaoudi, S. Joiret, M. Keddam, H. Takenouti, Electrochim. Acta 46 (2001) 2487–2498.
[48] M. Huang, Y.X. Zhang, F. Li, et al., Sci. Rep. 4 (2014) 3878.
[49] D.P. Zhao, M.Z. Dai, Y.L. Tong, X.F. Song, X. Wu, CrystEngComm 21 (2019) 5789–5796.
[50] P.H. Yang, Y. Ding, Z.Y. Lin, et al., Nano Lett. 14 (2014) 731–736.
[51] Q.Y. Gui, L.X. Wu, Y.Y. Li, J.P. Liu, Adv. Sci. (2019) 1802067.
[52] Y.F. Zhao, W. Ran, J. He, et al., Small 11 (2015) 1310–1319.
[53] Z.S. Wu, W.C. Ren, D.W. Wang, et al., ACS Nano 4 (2010) 5835–5842.
[54] Z.J. Fan, J. Yan, T. Wei, et al., Adv. Funct. Mater. 21 (2011) 2366–2375.
[55] Z.P. Li, Y.J. Mi, X.H. Liu, et al., J. Mater. Chem. 21 (2011) 14706–14711.
[56] K.P. Annamalai, X.S. Zheng, J.P. Gao, T.L. Chen, Y.S. Tao, Electrochim. Acta 144 (2019) 185–192.
[57] W. Wei, X. Cui, W. Chen, D.G. Ivey, Chem. Soc. Rev. 40 (2011) 1697–1721.
[58] X. Li, F. Zheng, D.F. Zhou, et al., Electrochim. Acta 289 (2018) 292–310.
[59] M. Li, B. Hua, J. Chen, Y.M. Zhong, J.L. Luo, Nano Energy 57 (2019) 186–194.
[60] J.K. Lee, H.M. Pathan, K.D. Jung, O.S. Joo, J. Power Sources 159 (2006) 1527–1531.
[61] W. Wang, S.R. Guo, I. Lee, et al., Sci. Rep. 4 (2014) 4452.
[62] Z. Chen, V. Augustyn, J. Wen, et al., Adv. Mater. 23 (2011) 791–795.
[63] Y.S. Hu, X. Liu, J.O. Müller, et al., Angew. Chem. Int. Ed. 48 (2009) 210.
[64] P. Jampani, O. Velikokhatnyi, K. Kadakia, et al., J. Mater. Chem. A 3 (2015) 8413–8432.
[65] H.Q. Liu, Y.P. Tang, C. Wang, et al., Adv. Funct. Mater. 27 (2017) 1606269.
[66] Y. Zhang, J. Lai, Y. Gong, et al., ACS Appl. Mater. Interfaces 8 (2016) 34309–34316.
[67] Y. Ya, B. Li, W. Guo, H. Pang, H.G. Xue, J. Power Sources 329 (2016) 148–169.
[68] Q.T. Qu, Y.S. Zhu, X.W. Gao, Y.P. Wu, Adv. Energy Mater. 2 (2012) 950–955.
[69] J.X. Zhu, L.J. Cao, Y.S. Wu, et al., Nano Lett. 13 (2013) 5408–5413.
[70] Z. Chen, V. Augustyn, J. Wen, et al., Adv. Mater. 23 (2011) 791–795.
[71] L.L. Xing, G.G. Zhao, K.J. Huang, X. Wu, Dalton Trans. 47 (2018) 2256–2265.
[72] L. Yao, C.R. Zhang, N.T. Hu, et al., Electrochim. Acta 295 (2019) 14–21.
[73] X. Zhou, Q. Chen, A.Q. Wang, et al., ACS Appl. Mater. Interfaces 8 (2016) 3776–3783.
[74] L.N. Gao, F.Y. Qu, X. Wu, J. Mater, Chem. A 2 (2014) 7367–7372.
[75] M.J. Qiu, P. Sun, L.X. Shen, et al., J. Mater. Chem. A 4 (2016) 7266–7273.
[76] Y. Liu, Y. Jiao, H.Y. Zhou, et al., Nano-Micro Lett. 7 (2015) 12–16.
[77] X. Xiao, T.P. Ding, L.Y. Yuan, et al., Adv. Energy Mater. 2 (2012) 1328–1332.
[78] P.A. Shinde, A.C. Lokhande, N.R. Chodankar, et al., Electrochim. Acta 224 (2017) 397–404.
[79] S.Y. Yao, F.Y. Qu, G. Wang, X. Wu, J. Alloys Compd. 724 (2017) 695–702.
[80] G.F. Cai, P. Darmawan, M.Q. Cui, et al., Adv. Energy Mater. 6 (2016) 1501882.
[81] X. Wu, S.Y. Yao, Nano Energy 42 (2017) 143–150.
[82] M.S. Zhu, W.J. Meng, Y. Huang, Y. Huang, C.Y. Zhi, ACS Appl. Mater. Interfaces 6 (2014) 18901–18910.
[83] F.M. Wang, X.Y. Zhang, Z.Z. Cheng, et al., Small 11 (2015) 749–755.

[84] A.K. Nayak, A.K. Das, D. Pradhan, ACS Sustain. Chem. Eng. 5 (2017) 10128–10138.
[85] Y. Jiao, Y. Liu, B.S. Yin, et al., Nano Energy 10 (2014) 90–98.
[86] Y. Zhong, Y.F. Ma, Q.B. Guo, et al., Sci. Rep. 7 (2017) 40927.
[87] X. Zheng, Y. Jiao, F. Chai, et al., J. Colloid Interface Sci. 457 (2015) 345–352.
[88] P. Wang, Z. Zheng, X. Cheng, et al., J. Mater. Chem. A 5 (2017) 19846–19856.
[89] Y. Zeng, M. Yu, Y. Meng, et al., Adv. Energy Mater. 6 (2016) 1601053.
[90] K.K. Lee, S. Deng, H.M. Fan, et al., Nanoscale 4 (2012) 2958–2961.
[91] J. Li, Y.W. Wang, W.N. Xu, et al., Nano Energy 57 (2019) 379–387.
[92] C. Guan, J.L. Liu, Y.D. Wang, et al., ACS Nano 9 (2015) 5198–5207.
[93] H.T. Sharifi, E. Gracia-Espino, H.R. Barzegar, et al., Nat. Commun. 4 (2013) 2319.
[94] X. Zheng, Z.C. Han, S.Y. Yao, et al., Dalton Trans. 45 (2016) 7094–7103.
[95] L.F. Chen, Z.Y. Yu, X. Ma, Z.Y. Li, S.H. Yu, Nano Energy 9 (2014) 345–354.
[96] X. Zheng, Z.C. Han, F. Chai, et al., Dalton Trans. 45 (2016) 12862–12870.
[97] C. Guan, J.L. Liu, Y.D. Wang, et al., ACS Nano 9 (2015) 5198–5207.
[98] Y.D. Dong, L. Xing, K.F. Chen, X. Wu, Nanomaterials 8 (2018) 487.
[99] H.W. Wang, Z.J. Xu, H. Yi, et al., Nano Energy 7 (2014) 86–96.
[100] Y. Li, J. Xu, T. Feng, et al., Adv. Funct. Mater. 27 (2017) 1606728.
[101] X. Lu, X. Chen, W. Zhou, Y. Tong, G. Li, A.C.S. Appl, Mater. Interfaces 7 (2015) 14843.
[102] J.W. Lee, T. Ahn, D. Soundararajan, J.M. Koc, J.D. Kim, Chem. Commun. 47 (2011) 6305–6307.
[103] Y.D. Dong, L. Xing, F. Hu, A. Umar, X. Wu, Mater. Res. Bull. 107 (2018) 391–396.
[104] K. Xie, J. Li, Y. Lai, et al., Electrochem. Commun. 13 (2011) 657–660.
[105] J. Huang, S. Yang, Y. Xu, et al., J. Electroanal. Chem. 713 (2014) 98–102.
[106] Y. Zeng, Y. Han, Y. Zhao, et al., Adv. Energy Mater. 5 (2015) 1402176.
[107] S. Sun, T. Zhai, C.L. Liang, S.V. Savilovc, H. Xia, Nano Energy 45 (2018) 390–397.
[108] L. Wang, H. Yang, X. Liu, et al., Angew. Chem. Int. Ed. 55 (2016) 1.
[109] Y. Zhu, S. Cheng, W. Zhou, et al., ACS Sustain. Chem. Eng. 5 (2017) 5067–5072.
[110] W.T. Sun, L. Xiao, X. Wu, F. Liu, J. Colloid Interf, Sci. 554 (2019) 705–710.
[111] Z. Yang, F. Xu, W. Zhang, et al., J. Power Sources 246 (2014) 24–31.
[112] H.H. Xiao, S.Y. Yao, H.D. Liu, et al., Prog. Nat. Sci. Mater. Inter. 26 (2016) 271–275.
[113] H.H. Xiao, F.Y. Qu, X. Wu, Appl. Surf. Sci. 360 (2016) 8–13.
[114] G.Q. Zhang, L. Yu, H.E. Hoster, X.W. Lou, Nanoscale 5 (2013) 877–881.
[115] W.T. Sun, L. Xiao, X. Wu, J. Alloys Compd. 772 (2019) 465–471.
[116] J.H. Kim, S.H. Kang, K. Zhu, et al., Chem. Commun. 47 (2011) 5214–5216.
[117] A.I. Inamdar, Y. Kim, S.M. Pawar, et al., J. Power Sources 196 (2011) 2393–2397.
[118] B. Wang, J.S. Chen, Z.Y. Wang, S. Madhavi, X.W. Lou, Adv. Energy Mater. 2 (2012) 1188–1192.
[119] S.I. Kim, J.S. Lee, H.J. Ahn, H.K. Song, J.H. Jang, A.C.S. Appl, Mater. Interfaces 5 (2013) 1596–1603.
[120] L.J. Li, J. Zhang, J.L. Lei, et al., J. Mater. Chem. A 6 (2018) 7099–7106.
[121] F. Luan, G.M. Wang, Y.C. Ling, et al., Nanoscale 5 (2013) 7984–7990.
[122] J.H. Lin, H.N. Jia, H.Y. Liang, et al., Adv. Sci. 5 (2017) 1700687.
[123] N.S. Liu, J. Li, W.Z. Ma, et al., ACS Appl. Mater. Interfaces 6 (2014) 13627–13634.
[124] W.P. Sun, X.H. Rui, J.X. Zhu, et al., J. Power Sources 274 (2015) 755–761.
[125] T.Y. Wei, C.H. Chen, H.C. Chien, S.Y. Lu, C.C. Hu, Adv. Mater. 22 (2010) 347–351.
[126] C.Y. Cao, W. Guo, Z.M. Cui, W.G. Song, W. Cai, J. Mater. Chem. 21 (2011) 3204–3209.
[127] K. Liang, X.Z. Tang, W.C. Hu, J. Mater, Chem. 22 (2012) 11062–11067.
[128] F. Meng, Z. Fang, Z. Li, et al., J. Mater. Chem. A 1 (2013) 7235–7241.
[129] P.F. Hu, Y. Liu, J.R. Song, X.F. Song, X. Wu, RSC Adv. 9 (2017) 32510–32516.
[130] X. Zhou, X. Shen, Z. Xia, et al., ACS Appl. Mater. Interfaces 7 (2015) 20322.
[131] Y.G. Li, M. Gong, Y.Y. Liang, et al., Nat. Commun. 4 (2013) 1805.
[132] L. Xing, Y.D. Dong, X. Wu, RSC Adv. 8 (2018) 28172–28178.
[133] L. Bao, T. Li, S. Chen, et al., Small 13 (2017) 1602077.
[134] Z.C. Han, X. Zheng, S.Y. Yao, et al., Appl. Surf. Sci. 365 (2016) 240–244.
[135] J. Fu, B. Zhu, C. Jiang, et al., Small 13 (2017) 1603938.
[136] X. Zheng, Z.C. Han, W.J. Yang, et al., Dalton Trans. 45 (2016) 16850–16858.
[137] Y. Lu, L. Li, D. Chen, G.Z. Shen, J. Mater. Chem. A 5 (2017) 24981–24988.
[138] X. Wu, Z.C. Han, X. Zheng, et al., Nano Energy 31 (2017) 410–417.
[139] L. Xing, Y.D. Dong, F. Hu, X. Wu, A. Umar, Dalton Trans. 47 (2018) 5687–5694.
[140] C. Li, J. Balamurugan, T.D. Thanh, N.H. Kim, J.H. Lee, J. Mater, Chem. A 5 (2017) 397–408.
[141] P. Wang, H. Zhou, C.F. Meng, et al., Chem. Eng. J. 369 (2019) 57–63.
[142] B. Wang, T. Zhu, H.B. Wu, et al., Nanoscale 4 (2012) 2145–2149.
[143] H. Pang, X.R. Li, Q.X. Zhao, et al., Nano Energy 35 (2017) 138–145.
[144] X. Bai, Q. Liu, J.Y. Liu, et al., Chem. Eng. J. 315 (2017) 35–45.
[145] W. Jiang, F. Hu, S.Y. Yao, Z.P. Sun, X. Wu, Mater. Res. Bull. 93 (2017) 303–309.
[146] P.F. Hu, D.P. Zhao, H.Q. Liu, K.F. Chen, X. Wu, CrystEngComm 21 (2019) 1600–1606.
[147] X.H. Qi, W.J. Zheng, G.H. He, et al., Chem. Eng. J. 309 (2017) 426–434.
[148] D.P. Zhao, M.Z. Dai, H.Q. Liu, et al., Cryst. Growth Des. 19 (2019) 1921–1929.
[149] L. Huang, G.H. Waller, Y. Ding, et al., Nano Energy 11 (2015) 64–70.
[150] D.P. Zhao, M.Z. Dai, H.Q. Liu, et al., Adv. Mater. Interfaces 6 (2019) 1901308.
[151] C.Z. Yuan, J.Y. Li, L.R. Hou, et al., Adv. Funct. Mater. 22 (2012) 4592–4597.
[152] F.X. Ma, L. Yu, C.Y. Xu, X.W. Lou, Energy Environ. Sci 9 (2016) 862–866.
[153] H. Wang, H. Yi, X. Chen, X. Wang, J. Mater. Chem. A 2 (2014) 1165–1173.
[154] C. Liu, W. Jiang, F. Hu, X. Wu, D.F. Xue, Inorg. Chem. Front. 5 (2018) 835–843.
[155] L. Xu, Y. Zhao, J.B. Lian, et al., Energy 123 (2017) 296–304.
[156] B. Liu, B.Y. Liu, Q.F. Wang, et al., ACS Appl. Mater. Interfaces 5 (2013) 10011–10017.
[157] L.F. Shen, Q. Che, H.S. Li, X.G. Zhang, Adv. Funct. Mater. 24 (2014) 2630–2637.
[158] X.S. Feng, Y. Huang, C. Li, et al., Chem. Engn. J. 368 (2019) 51–60.
[159] A.G. Pandolfo, A.F. Hollenkamp, J. Power Sources 157 (2006) 11–27.
[160] W.Q. Ma, H.H. Nan, Z.X. Gu, B.Y. Geng, X.J. Zhang, J. Mater. Chem. A 3 (2015) 5442–5448.
[161] C. Liu, X. Wu, H. Xia, CrystEngComm 20 (2018) 4735–4744.
[162] Y. Liu, Z.B. Wang, Y.J. Zhong, et al., Adv. Funct. Mater. 27 (2017) 1701229.
[163] B. Jai, G.L. Nagaraju, B. Ramulu, S.C. Sekhar, J.S. Yu, Electrochim. Acta 299 (2019) 509–517.
[164] S.H. Yue, H. Tong, L. Lu, et al., J. Mater. Chem. A 5 (2017) 689–698.
[165] J. Hu, M.C. Li, F.C. Lv, et al., J. Power Sources 294 (2015) 120–127.
[166] D.P. Zhao, H.Q. Liu, X. Wu, Nano Energy 57 (2019) 363–370.
[167] M.Z. Dai, D.P. Zhao, H.Q. Liu, et al., Sci. Adv. Mater. 11 (2019) 1100–1105.
[168] X.X. Jia, X. Wu, B.D. Liu, Dalton Trans. 47 (2018) 15506–15511.
[169] M.C. Liu, L.B. Kong, C. Lu, et al., J. Mater. Chem. A 1 (2013) 1380–1387.
[170] D. Guo, P. Zhang, H. Zhang, et al., J. Mater. Chem. A 1 (2013) 9024–9027.
[171] M.C. Liu, L. Kang, L.B. Kong, et al., RSC Adv. 3 (2013) 6472–6477.
[172] Y.L. Tong, B.Q. Chi, D.L. Qi, X.Y. Liu, Sci. Adv. Mater. 11 (2019) 338–344.
[173] Q. Yang, Z. Lu, X. Sun, J. Liu, Sci. Rep. 3 (2013) 3537.
[174] Z.X. Gu, R.F. Wang, H.H. Nan, B.Y. Geng, X.J. Zhang, J. Mater. Chem. A 3 (2015) 14578–14584.
[175] H.Q. Liu, D.P. Zhao, P.F. Hu, et al., Chem. Eng. J. 373 (2019) 485–492.
[176] X.Z. Yu, B.G. Lu, Z. Xu, Adv. Mater. 26 (2014) 1044–1051.